Title

Metal-Dependent Activity of Fe and Ni Acireductone Dioxygenases: How Two Electrons Reroute the Catalytic Pathway

Journal

Journal of Molecular Biology, 425(16)

ISSN

0022-2836

Authors

Sparta, Manuel
Valdez, Crystal E
Alexandrova, Anastassia N

Publication Date

2013-08-01

DOI

10.1016/j.jmb.2013.05.001

Peer reviewed

jmb Article

Metal-Dependent Activity of Fe and Ni Acireductone Dioxygenases: How Two Electrons Reroute the Catalytic Pathway

Manuel Sparta†, Crystal E. Valdez† and Anastassia N. Alexandrova

Department of Chemistry and Biochemistry, *University of California, Los Angeles, Los Angeles, CA 90095-1569, USA*

Correspondence to Anastassia N. Alexandrova: *ana@chem.ucla.edu*
http://dx.doi.org/10.1016/j.jmb.2013.05.001
Edited by D. Case

Abstract

Two virtually identical acireductone dioxygenases, ARD and ARD′, catalyze completely different oxidation reactions of the same substrate, 1,2-dihydroxy-3-keto-5-(methylthio)pentene, depending exclusively on the nature of the bound metal. Fe^{2+}-dependent ARD′ produces the α-keto acid precursor of methionine and formate and allows for the recycling of methionine in cells. Ni^{2+}-dependent ARD instead produces methylthiopropionate, CO, and formate, and exits the methionine salvage cycle. This mechanistic difference has not been understood to date but has been speculated to be due to the difference in coordination of the substrate to Fe^{2+} *versus* Ni^{2+}: forming a five-membered ring *versus* a six-membered ring, respectively, thus exposing different carbon atoms for the attack by O_2. Here, using mixed quantum-classical molecular dynamics simulations followed by the density functional theory mechanistic investigation, we show that, contrary to the old hypothesis, both metals preferentially bind the substrate as a six-membered ring, exposing the exact same sites to the attack by O_2. It is the electronic properties of the metals that are then responsible for the system following different reaction paths, to yield the respective products. We fully explain the puzzling metal-induced difference in functionality between ARD and ARD′ and, in particular, propose a new mechanism for ARD′. All results are in agreement with available isotopic substitution and other experimental data.

Introduction

The two acireductone dioxygenases (ARD and ARD′) are found in the methionine salvage pathway in living organisms, including humans.[1,2] It is intriguing that these two enzymes, while sharing the same protein sequence and differing only by the nature of the bound metal, catalyze completely different reactions of oxidation of the same substrate, 1,2-dihydroxy-3-keto-5-(methylthio)pentene.[3,4] The Ni^{2+}-dependent enzyme, ARD (EC 1.13.11.53), catalyzes the formation of formate, methylthiopropinate, and carbon monoxide, whereas the Fe^{2+}-dependent enzyme, ARD′ (EC 1.13.11.54), promotes the formation of formate and 2-keto-4-methylthiobutyric acid (precursor of methionine).[3] Furthermore, it has been demonstrated that the two enzymes have the active sites with identical pseudo-octahedral coordination of the metal centers, by His96, His98, Glu102, and His140, with the remaining two positions being occupied by either water molecules or the substrate.[5,6] Finally, it has been shown that it is possible to reconstitute either of the enzymes by combining the apoprotein with a solution containing the proper metal.[7] Hence, although Fe^{2+} and Ni^{2+} have different binding constants, the protein does not preferentially bind either one of the cations.

Sequential reaction mechanisms have been proposed for both enzymes. Shown by kinetic analyses, a red λ_{max} shift that occurs upon substrate binding in anaerobic conditions to ARD and ARD′ suggests that the substrate binds as a dianion to the enzymes.[5] The dianionic substrate is electron rich and susceptible to electrophilic attack by dioxygen, as confirmed by the non-enzymatic reaction studies. In the absence of metal ions, the oxidation of 1,2-dihydroxy-3-keto-5-(methylthio)pentene yields the same products as ARD′ via a base-catalyzed

oxidative cleavage, indicating that dioxygen activation is not needed for enzymatic activity.[6] Other studies have shown that non-heme iron proteins, in particular non-heme iron dioxygenases, require metal activation of dioxygen,[8,9] whereas in the presence of dioxygen alone, both ARD and ARD′ do not bind oxygen, further proving the requirement of sequential binding of the substrate followed by dioxygen binding for catalysis.[6]

The exact mechanisms of the two reactions remain unknown. However, using isotopically labeled dioxygen and following the incorporation in the products, it has been postulated that the substrate may coordinate the metal center forming either a five- or six-membered ring, depending on the metal present. This would dictate different targets for the attack by dioxygen, with the subsequent cleavage of the C1–C2 bond (in ARD′), or the C1–C2 and C2–C3 bonds (in ARD) (Scheme 1). Isotopic studies have shown that dioxygen is incorporated into the products.[10,11] To the best of our knowledge, the catalytic mechanisms have never been investigated theoretically. On the other hand, the uncatalyzed reaction of the substrate with dioxygen has been investigated by Borowski *et al.*[12] by means of density functional theory (DFT) calculations and experimentally by Dai *et al.*[6] These studies concluded that the uncatalyzed reaction may occur via a radical mechanism. As shown by Dai *et al.*,[6] using a substrate modified with a radical trap, a mechanism involving long living radicals is not likely to occur during the catalyzed reaction.

In this article, we report on the first theoretical study of the catalytic cycles promoted by ARD and ARD′. We first address the acireductone substrate binding to the two proteins and show that, contrary to the old belief, there is no difference in the binding mode of acireductone to ARD and ARD′. To show this, we use our new method for dynamics simulations of metalloproteins, QM/DMD.[13] We then tackle the catalytic mechanisms of ARD/ARD′ using first-principle calculations and show that the bifurcation of the mechanism occurs later in the reaction route. We propose a new catalytic mechanism for ARD′, which includes an additional intermediate, as compared to the ARD pathway. This difference is due to just two extra electrons available in Ni^{2+} *versus* Fe^{2+} and the resultant RedOx flexibility of Fe^{2+}. This allows for the rerouting of the reaction. As we were preparing this article, Allpress *et al.*[14] experimentally showed that in a bioinorganic complex mimicking ARD and ARD′, the regioselectivity change of aliphatic carbon–carbon cleavage is also not dependent on the substrate binding mode, but rather dependent on the intermediate in the reaction pathway, an intermediate found in this study. Although their experiments used a non-native substrate, our results agree with the trends of their experiments.

Results and Discussion

ARD and ARD′ bind the substrate in the same way

It has been long speculated that the key difference between the mechanisms of ARD and ARD′ is the binding modes of the substrate to the metals: the substrate would coordinate to Fe^{2+} with the O_1 and O_2, hence forming a five-membered ring, whereas to Ni^{2+}, it would bind with O_1 and O_3, producing a six-membered ring (see Scheme 1 for atom numeration). This difference in binding should indeed lead to the respective products. However, we challenge this speculation. The two proteins share the exact same sequence. The bond lengths to Fe^{2+} and Ni^{2+} could be slightly different, but this does not seem enough to change the binding pose so dramatically.

To address whether or not there is a dependence of the binding mode on the nature of the metal, we performed QM/DMD simulations for both metal

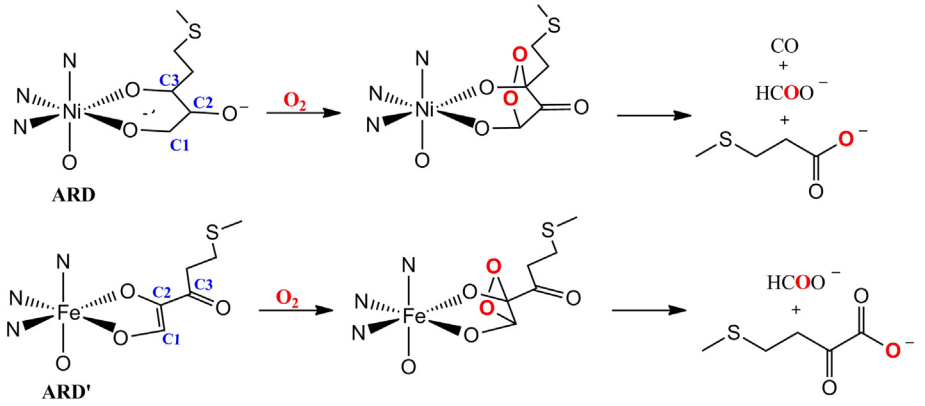

Scheme 1. The old hypothesis for the reaction mechanisms of oxidation of acireductone catalyzed by ARD and ARD′. The suspected difference in the substrate binding is illustrated.

variants, and for two different binding modes, that is, a total of four simulations. The lowest energy spin states were found on the cluster models of the two active sites (triplet for Ni ARD and quintet for Fe ARD′), and the QM/DMD simulations on the entire protein with these spin states were performed. In Fig. 1a and b, we report the QM and DMD energies for the Ni^{2+} containing ARD coordinating the substrate as a six-membered ring (in red) and five-membered ring (in black), as a function of the iteration number. Both energies show a clear and consistent preference for the six-membered ring coordination. Figure 1c and d depict representative structures of the active site with the substrate coordinated in the two different modes, as resulted from QM/DMD simulations. Thus, for ARD, the old hypothesis about the binding mode is fully confirmed.

However, for ARD′, there is also a clear preference for the six-membered ring coordination, as follows from the QM and DMD energies produced in QM/DMD simulations (Fig. 2a and b). From just the QM energies of the active site, the five-membered ring coordination is discouraged by ca. 10 kcal/mol. This result contradicts the old hypothesis that Fe^{2+} promotes the five-membered ring coordination.

In both ARD and ARD′, coordination as a six-membered ring indeed makes sense from the structural point of view. Arg154 in the second coordination sphere of the metal forms an H-bond to the substrate O_2 atom, stabilizing this coordination mode for both ARD and ARD′ (Figs. 2d and 3d). In the five-membered ring scenario, this interaction is impossible (Figs. 2c and 3c). The overall structures of the binding pocket upon the substrate binding are also exceptionally consistent between the ARD and ARD′ forms of the protein. Experimental data for the ARD and ARD′ enzyme–substrate adducts are limited. However, similar UV–Vis absorption of these adducts indicated that there may not be a difference in binding mode of ARD and ARD′.[13] We performed the time-dependent DFT calculations on the substrate coordinated to ARD and ARD′ in the two studied orientations and in solution (Supplementary Information). It is noteworthy that, in solution, the five-membered ring-like conformation of the substrate is preferred by ca. 5 kcal/mol. Our

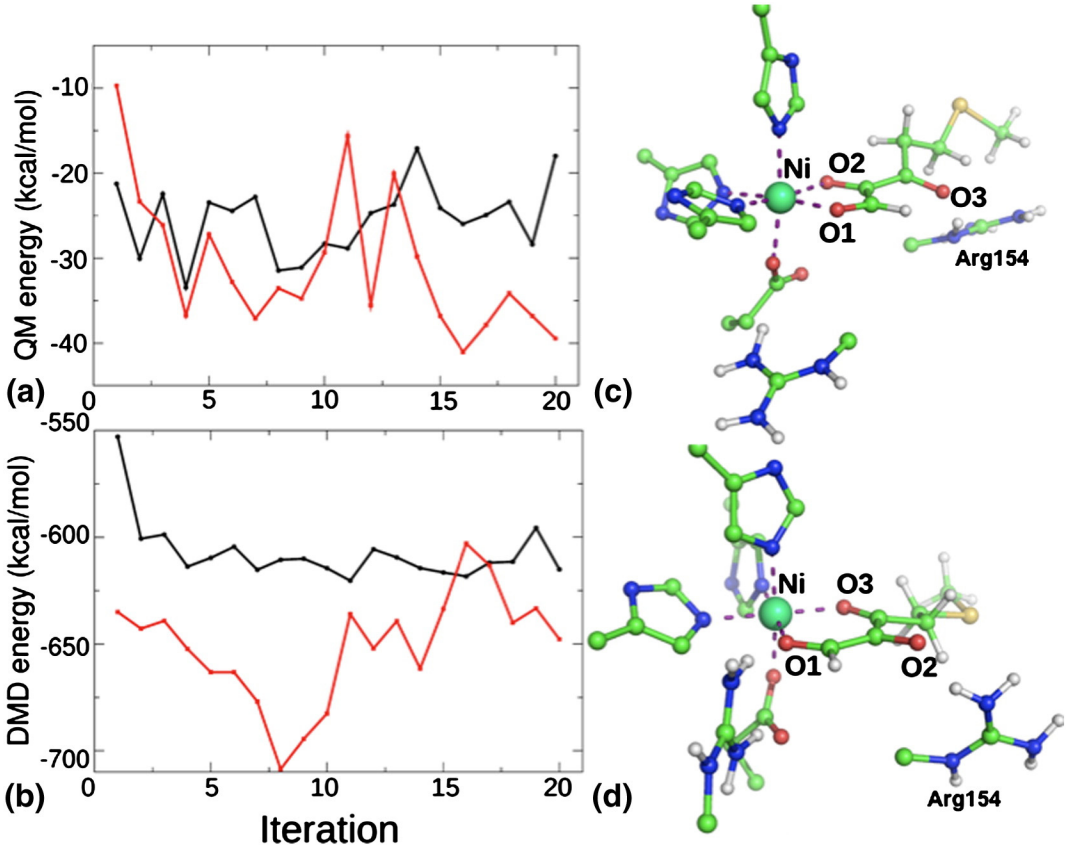

Fig. 1. Results of QM/DMD simulations for the Ni^{2+} containing ARD coordinating the substrate in two different ways. (a and b) The QM and DMD energies, respectively, plotted as a function of the iteration number. The red lines correspond to the six-membered ring coordination, and the black lines correspond to the five-membered ring coordination. The preference for the six-membered ring binding is apparent. (c and d) Representative structures of the active site with the substrate coordinated as five- and six-membered rings, respectively.

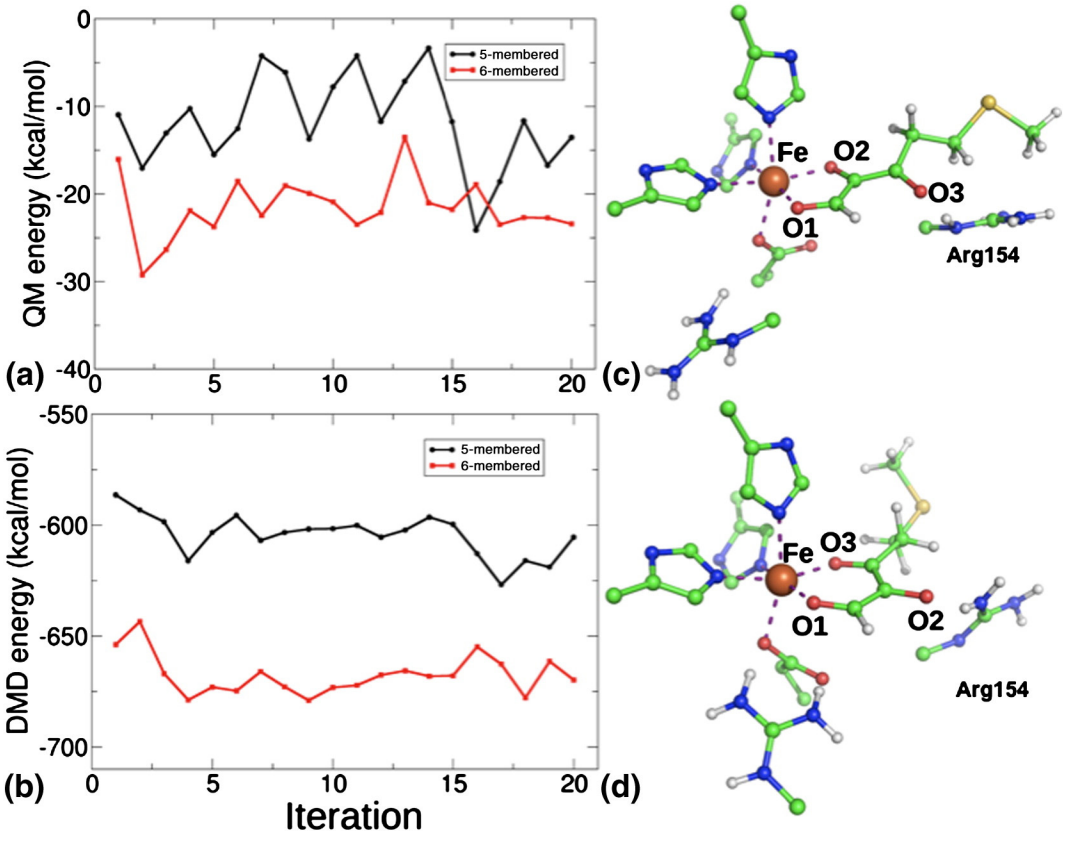

Fig. 2. Results of QM/DMD simulations for the Fe^{2+} containing ARD′ coordinating the substrate in two different ways. (a and b) The QM and DMD energies, respectively, plotted as a function of the iteration number. The red lines correspond to the six-membered ring coordination, and the black lines correspond to the five-membered ring coordination. The preference for the six-membered ring binding is again apparent. (c and d) Representative structures of the active site with the substrate coordinated as five- and six-membered rings, respectively.

results indicate that both coordination modes result in similar red shift in the UV–Vis spectra, and so from the computational spectroscopy standpoint, the two modes are also indistinguishable.

It was brought to our attention at the stage of the revision that, in the earlier work by Ju *et al.*,[15] classical molecular dynamics simulations were performed on the two metal variants of ARD, with the metal coordination kept fixed at the geometry observed in XAS experiments. Ten-picosecond dynamics simulations showed that Trp162 "guarding" the entryway to the binding site of ARD changed its conformation depending on the bound metal. It is "closed" in ARD interacting with the substrate and supposedly stabilizing the six-membered ring binding, but "open" in the ARD′, thereby facilitating the different binding mode. We performed extensive (ca. 100 ns) QM/DMD simulations on the Fe and Ni of the protein using the 1ZRR and 2HJI structures. The metals were treated quantum mechanically and their coordination was allowed to move in the dynamics. We found very little difference in the position of the C-terminus of the protein and specifically Trip162 for the Ni and Fe forms. Results are given in the Supplementary Information. Therefore, we expect the possible weak dispersion interaction of the substrate with Tri162 to play no or very little role in defining the substrate binding. Instead, Arg154 appears to drive the preference for the six-membered ring coordination. In fact, if Arg154 is excluded from the shared QM-DMD domain in the simulations, the preference becomes less clear.

Catalytic mechanism for ARD and ARD′

For mechanistic studies, the lowest QM energy structure was chosen from each of the QM/DMD simulations. We do not explicitly consider the barrier toward the dioxygen attack, since the difference between ARD and ARD′ is rooted in the later steps along the reaction profile.

For ARD, the lowest energy spin state unequivocally is a triplet. However, other spin states were also considered. The dotted lines on Fig. 3 connect stationary points along the reaction paths without the consideration of possible spin crossover. The reaction proceeds as follows: dioxygen binds to C1

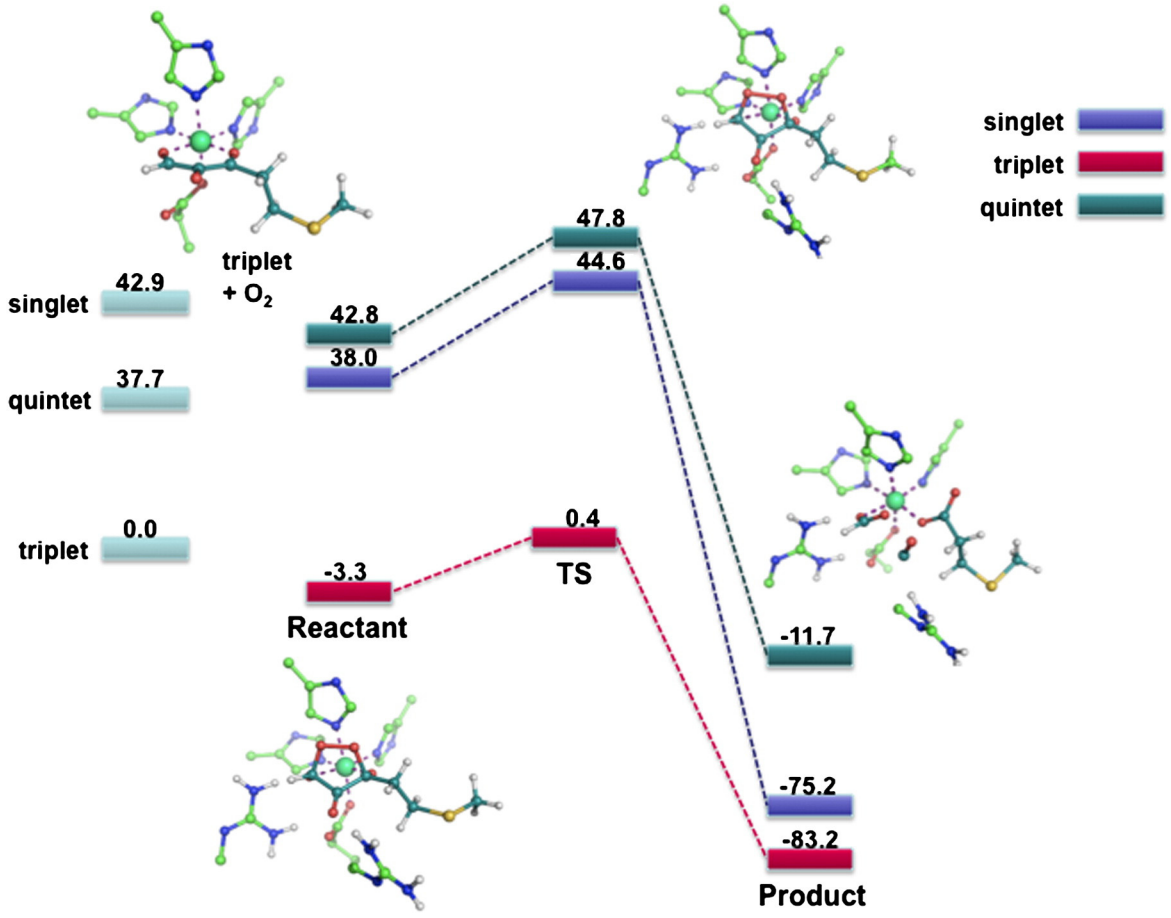

Fig. 3. Reaction profile for the Ni^{2+} containing ARD. All numbers are calculated with TPSSh/def2-TZVPP.

and C3 of the substrate forming a dioxygen adduct. The lowest energy state for this adduct is a triplet with other states being considerably higher in energy (Fig. 3). In order to start from the triplet state of the initial complex and reach the triplet potential energy surface in the intermediate, the system has to undergo the spin crossover, which is anticipated to be a facile process, considering the typically large magnitudes of the spin orbit coupling in the octahedral complexes of Ni^{2+}. The intermediate then has access to the low-barrier transition state in which dioxygen splits, and the substrate synchronously dissociates into the three products, carbon monoxide and two carboxylate products (Fig. 3). Both the transition state and the products are triplets, with the singlet and the quintet being much higher in energy.

For ARD′, the mechanism contains an intermediate step that is not seen in ARD. Firstly, the starting complex has the splitting between the spin states that is much smaller than that in ARD. The quintet state is preferred by ca. 10 kcal/mol. The same dioxygen adduct is formed when dioxygen binds to C1 and C3 on the substrate. This intermediate is lower in energy than the reactants only on the quintet potential energy surface, with the singlet and the triplet being ca. 10 kcal/mol above it and the septet being 20 kcal/mol higher. Getting to the singlet state from the initial quintet requires spin crossing, which is very typical for Fe^{2+}. The reaction proceeds with the splitting of dioxygen. However, unlike in ARD, on all but the singlet surface, the split leads to a new intermediate where the O–O bond is dissociated but with the reactants still being attached to the complex (Fig. 4). The intermediate is 16–25 kcal/mol below the reactants. On the singlet surface, the split of the dioxygen leads to the three ARD (Ni-like) products without a barrier. Since these products are not observed experimentally, we are forced to conclude that after the first intermediate, the higher-energy singlet and also the septet surfaces are not reachable in this reaction. The reaction must proceed on the lower-energy quintet or triplet surfaces. Both of these states have an access to the low-energy epoxy-like transition state with oxygen attached to C3 transferring to C2. After this transition state, the system splits spontaneously to form the two ARD′ products, an alpha-keto carboxylate and

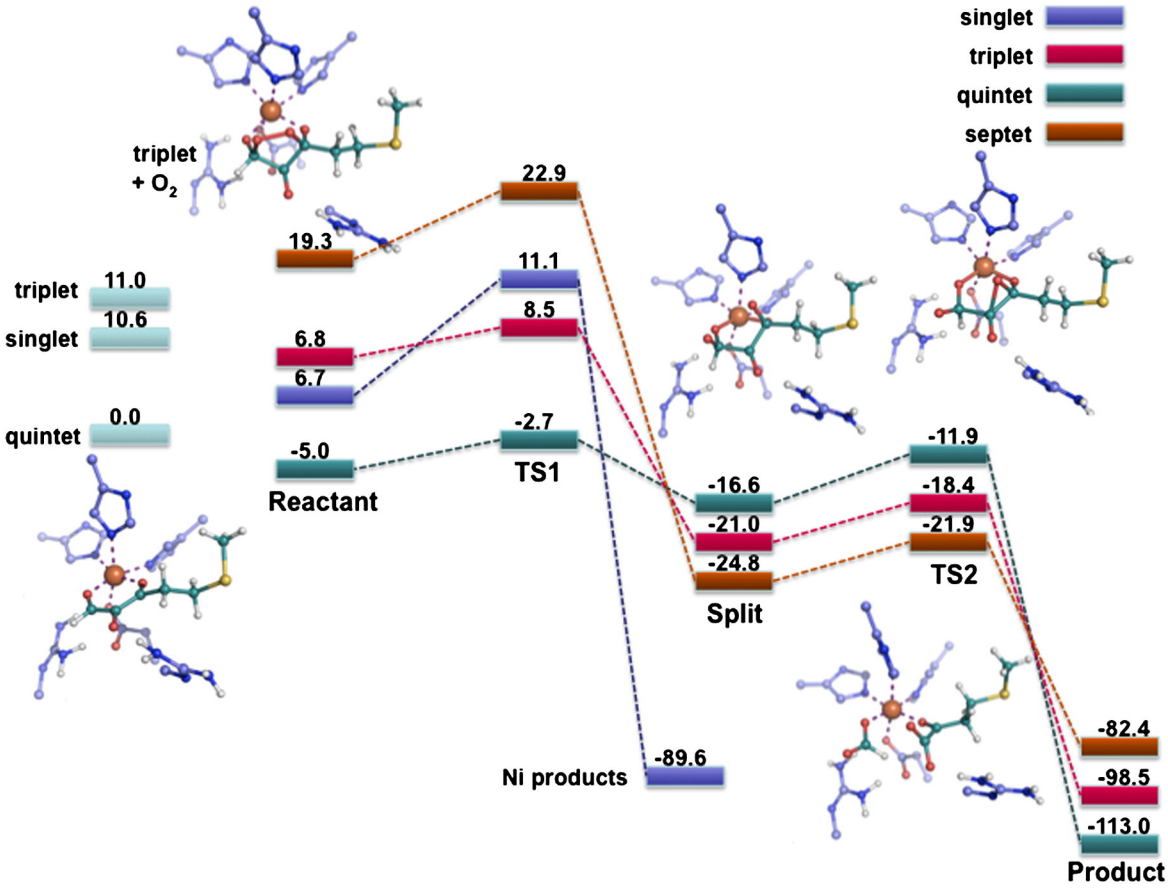

Fig. 4. Reaction profile for the Fe^{2+} containing ARD′. All reported numbers are calculated with TPSSh/def2-TZVPP.

formate. Remarkably, in the recently published work on inorganic complexes mimicking ARD and ARD′, it was suggested that the Fe form of this catalyst has to have an additional intermediate along the reaction path.[13] This is in full agreement with our findings for ARD′.

Considering the QM energy difference between the six-membered ring coordination mode and the five-membered ring coordination mode to ARD′ being ca. 10 kcal/mol, we decided to still check the reaction mechanism for the five-membered ring coordination. In this process, dioxygen must attack the substrate at the C1 and C2 position, generating a strained four-membered cycle: C1–C2–O–O. All attempts to find the minimum on the potential energy surface for this structure failed. Dioxygen does not attach to the substrate in this fashion. Therefore, indeed, the old mechanism postulated for ARD′ appears to be incorrect.

The key conclusion of this section is that the difference in reaction mechanisms between ARD and ARD′ does not have to be dictated by the binding mode. Instead, the differentiation happens further along the reaction profile, during the splitting of dioxygen. This has to be caused by the electronic properties of the bound metal (Fig. 5). In the next section, we investigate this difference in detail.

Why does ARD′ have extra intermediate, whereas ARD does not?

The crucial bifurcation point in the reaction mechanism is the moment when dioxygen splits, producing either the ARD-like products or an additional intermediate (in the case of ARD′). The reason for this difference must be rooted in the electronic properties of the metal. To answer this question of why ARD′ passed through a split dioxygen intermediate before proceeding to the products whereas ARD does not, we performed natural population analysis (NPA)[16] calculations of the partial charges on all the stationary points of the lowest energy spin state for both proteins (Tables 1 and 2).

For ARD, as the system progresses through to the transition state where dioxygen splits, there is no significant charge transfer occurring between the substrate, metal, and side chains. At the final product formation stage, the charge redistribution takes place within the bound substrate with dioxygen

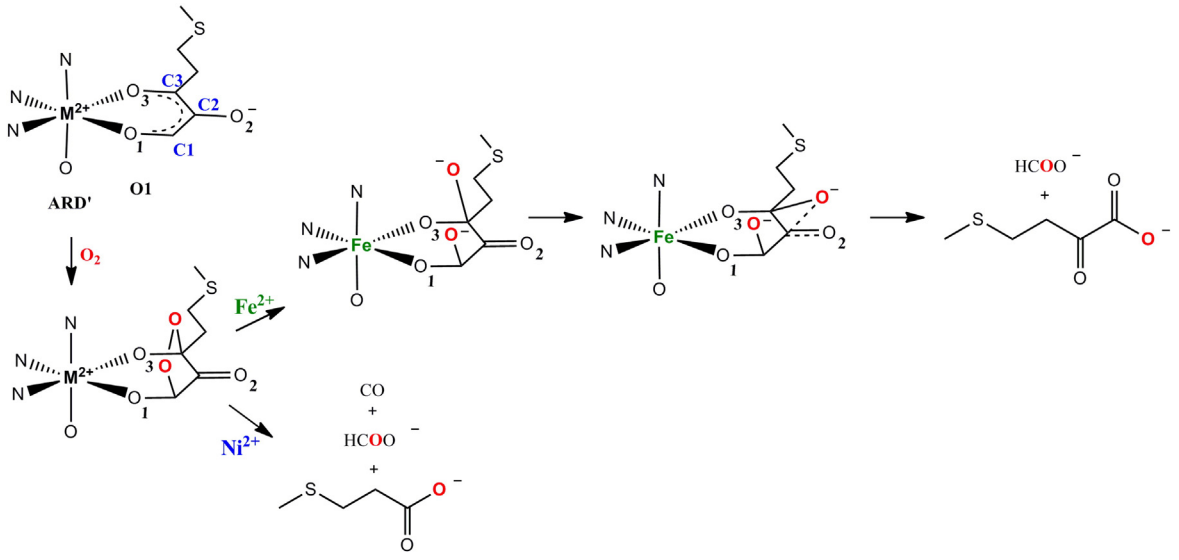

Fig. 5. The new proposed mechanisms for ARD and ARD′.

attached (Table 1). Ni does not participate in any charge transfer to and from the substrate. Ni in ARD thus plays merely a Lewis acid role; it coordinates and polarizes the substrate, but it has no RedOx role in the reaction.

For ARD′, the situation is different and more complicated (Table 2). Upon binding and splitting of dioxygen, the substrate gains the partial negative charge. NPA shows that the electrons are drawn from the protein residues coordinating the Fe ion. The charge on Fe itself does not change. This can be seen from comparing all the charges from the reactants' stationary point to the split intermediate: the positive charge on all the residues and the negative change on O_2 increase. Donation of electrons to the attached dioxygen populates its formerly π*-orbital, thus leading to its split. Then, upon the formation of products, the substrate donates electrons back to Fe, which transmits them to the side chains coordinating it (Table 2). The RedOx flexibility of Fe facilitates the process of O_2 splitting, which requires additional electrons. Ni, having a fuller *d*-shell of atomic orbitals, is not nearly versatile. It is indeed not in vain that electron transport proteins typically contain Fe and Fe–S centers. What is unusual about ADR′ is that Fe is coordinated by His residues, and not the usual Cys utilized in electron transporters, and yet Fe in ADR′ pulls electrons out of His in the course of the reaction.

The difference in how ARD and ARD′ interact with the substrate can also be detected from the geometries of the bound complexes. In ARD, the distances from the Ni cation to the O_1 and O_3 atoms of the substrate are 2.00 and 2.19 Å. In ARD′, the coordination to the metal is much tighter: the same distances read 1.86 and 1.91 Å. The closer coordination to Fe^{2+} is again a manifestation of more "openings" in the set of *d*-AOs of the metal for *s*-donation from the substrate. Thus, stronger and more RedOx active interaction is observed. The electron donation to dioxygen is responsible for the stabilization of the second intermediate along the reaction profile of ARD′. Therefore, the rerouting of the catalytic mechanism between ARD and ARD′ is exclusively due to the differences in the electronic properties of the metal.

Conclusions

Oxidation of 1,2-dihydroxy-3-keto-5-(methylthio) pentene by ARD and ARD′ has important implications in biology. This enzyme either facilitates recycling of methionine in living cells or exits this

Table 1. NPA charges on the side chains, the Ni ion, the substrate, and the attached O_2 in ARD

	His96	His98	Glu102	Arg104	His140	Arg154	Ni^{2+}	Substrate	O_2
Reactant	0.09	0.09	−0.85	0.87	0.09	0.93	1.40	−0.97	−0.65
TS	0.09	0.09	−0.84	0.87	0.09	0.93	1.40	−0.95	−0.67
Product	0.07	0.10	−0.83	0.87	0.09	0.98	1.40	−0.22	−1.45

Throughout the reaction mechanism, charges do not vary, indicating that the Ni atom does not donate or receive any electron density from the substrate. All charges are computed with TPSSh/def2-TZVPP.

Table 2. NPA charges on the side chains, the Fe ion, the substrate, and the attached O_2 in ARD′

	His96	His98	Glu102	Arg104	His140	Arg154	Fe^{2+}	Substrate	O_2
Reactant	0.08	0.07	−0.82	0.88	0.06	0.94	1.46	−1.00	−0.66
TS1	0.08	0.07	−0.82	0.88	0.06	0.94	1.45	−0.98	−0.68
Split	0.13	0.15	−0.79	0.90	0.15	0.94	1.48	−0.66	−1.30
TS2	0.13	0.16	−0.79	0.90	0.16	0.93	1.50	−0.65	−1.34
Product	0.07	0.10	−0.81	0.90	0.09	0.92	1.47	−0.33	−1.41

Upon splitting of the O_2, the attached O_2 draws the negative charge from the ligands coordinating Fe. All charges are computed with TPSSh/def2-TZVPP.

recycling pathway. Fe^{2+}-dependent ARD′ produces the α-keto acid precursor of methionine and formate, whereas Ni^{2+}-dependent ARD instead produces methylthiopropionate, CO, and formate. The way by which the two proteins do it solely due to the nature of the bound metal has been a long-standing mystery. However, it has been speculated that the mechanistic difference stems from the differences in the binding of the substrate to ARD *versus* ARD′. In this work, we show that this old hypothesis does not hold up. Both proteins bind the substrate in the same way: as a six-membered ring, via attaching O_1 and O_3 to the metal (as in Fig. 1d). This was shown with the use of our powerful hybrid dynamics methods, QM/DMD. The subsequent mechanistic study revealed that the determination of the final products happens later in the reaction, after dioxygen attacks the bound substrate. Upon splitting of dioxygen, ARD immediately decomposes the reacting system into its three experimentally found products. Contrastingly, ARD′ passes through an additional split dioxygen intermediate and then proceeds through an epoxy-like transition state with a small activation energy to the two products. The ability of ARD′ to stabilize an additional intermediate and thus produce the two products is due to the RedOx flexibility of the Fe^{2+} as compared to the more electron-rich Ni^{2+}. Fe^{2+} transmits electrons from the residues, coordinating it to bound dioxygen and populating its formerly p*-orbital. This leads to dioxygen splitting in the second intermediate and eventual access to the ARD′ reaction route. It is remarkable how just two additional electrons on the metal center in ARD *versus* ARD′ cause a dramatic mechanistic difference. All findings are in agreement with the available spectroscopic and isotope labeling data. This is the first time the mechanisms of ARD and ARD′ have been explicated.

Theoretical Methods

The initial structures of ARD/ARD′ were obtained from the Protein Data Bank (PDB) (ARD PDB code: 1ZRR,[17] ARD′ PDB code: 2HJI[15]). However, to examine specifically the metal-dependent effects on the mechanism, we only used one PDB structure, 2HJI, for the QM/DMD simulations using Fe and Ni. Since neither of the PDB structures contained the coordinated substrate, 2-dihydroxy-3-keto-5-methylthiopentene, it was manually built into the protein. The coordination geometry chosen for each structure comes from experimental and theoretical predictions.[4,11]

QM/DMD simulations

This study employs the recently developed QM/DMD[12] method, where DMD is short for discrete molecular dynamics.[18–21] QM/DMD is a hybrid method, a variant of QM/MM,[15,18,19] which efficiently captures metalloprotein dynamics on the order of tens of nanoseconds, in conjunction with the quantum mechanical description of the active site. It has been shown to perform exceptionally well for recapitulating and recovery of native protein structures down to the subtle structural details at the active sites,[12] electronic properties of the bound metals,[12,22] protein conformational responses to substrate binding and metal replacement,[21–24] and mechanistic studies of enzymatic reactions.[21,22] The main attractive feature of QM/DMD is its affordability as compared to that of other often equally capable QM/MM methods. The strength of the method is in part due to DMD,[15,18–20] a remarkably successful classical force-field-based method for sampling biological molecules and their complexes. No explicit solvent is used in DMD, but solvation is included in the averaged way into the force field in use.

DMD samples most of the protein, except for the immediate coordination of the metal. In this way, there is no need for the parameterization of the force field to describe the metal, which is then free to change the coordination environment in the course of the simulation. The QM part of the simulations consists of periodic relaxations following the *ab initio* gradients for nuclear motions of the larger active site that includes the metals, their ligands, and the substrate, and may include other important amino acids near the reactive center. The QM/DMD boundary is thus “breathing” and goes around just the metal and its immediate coordination or around the larger active site, depending on the stage of the simulation, as described below. The presence of the shared QM and DMD domain permits for the simple and efficient communication between the QM and

DMD regions. We use QM/DMD to test the current hypothesis on the preferred binding modes of the substrate to ARD and ARD′.

QM/DMD partitioning the protein

The coupling between QM and DMD in the QM/DMD methods is achieved via partitioning the whole system into three domains and then using the breathing QM-DMD boundary that circumvents parts of the protein significantly different in size, depending on the stage of the simulation. Figure 6a shows how the protein is divided into three domains. The metal cation, Ni for ARD and Fe for ARD′, and the portion of the active site immediately surrounding it constitute the *QM-only* domain, which moves only during the QM phase of the simulation and is not allowed to be moved by classical DMD. The larger active site shown in purple in Fig. 6a and zoomed in in Fig. 6b is the shared *QM-DMD* domain, which can be moved by both QM and DMD, depending on the stage of the run. The *QM-DMD* domain is a minimalistic, chemically meaningful cluster model of the active site. It includes the metal ion, His96, His98, His140, Glu102, doubly deprotonated substrate, and two protonated Arg104 and Arg154 that stabilize the substrate through H-bonds. The truncation of the amino acids in the QM calculations occurred at the C^{α}–C^{β} bond, C^{δ}–C^{γ} for arginines. Whenever a bond is truncated, the atom included in the QM region is saturated with a hydrogen atom positioned along the original bond at a distance equal to 0.7052*R(C – C/N). All saturating hydrogens and their bond partners were frozen during the QM optimization of the active site to retain the geometry imposed by the rest of the protein. Furthermore, additional constraints were imposed to prevent any of the residues coordinating the metal to become too distorted and lose their coordination during DMD phases. A few atoms near the metal centers in the active site were allowed to be sampled by DMD only within ±0.01 Å from the values predicted by QM. Those atoms are the two C atoms adjacent to N coordinating the metal in the His residues, and Cg of Glu102. This set of constraints was developed and validated in our previous works.[12,21–23] The rest of the system, including most of the protein macromolecule and a large portion of ARD, constitutes the *DMD-only* domain.

Simulation details

Each simulation starts from a short DMD run of 1000 DMD time units (t.u.), where 1 t.u. roughly corresponds to 50 fs, at a temperature of T = 0.10 kcal/(mol*K), with a high heat exchange rate of the protein with the bath for 10 $t.u.^{-1}$, using an Andersen thermostat.[25] This was found to remove clashes introduced by the PDB starting structures.[26] Then, the QM/DMD simulation on the prepared protein begins. It proceeds in an iterative fashion, where the DMD and QM machineries alternate. It

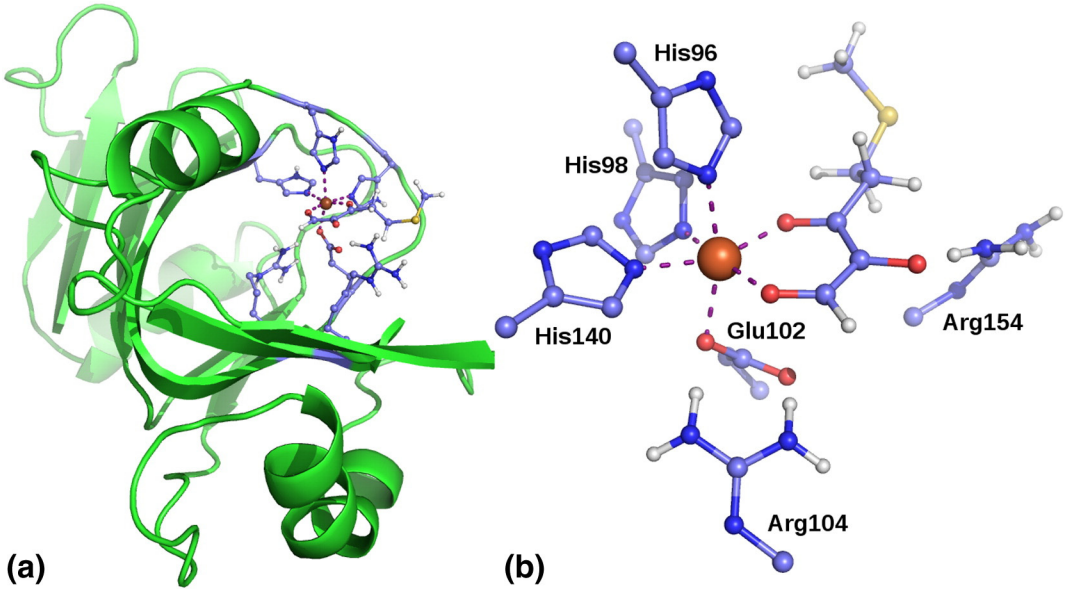

Fig. 6. (a) Schematic representation of the QM/DMD domains. The atoms directly coordinated to the metal are the *QM-only* domain, the purple area defines the *QM-DMD* domain, and the rest of the system constitutes the *DMD-only* domain. Protein backbone is shown as thick green lines. (b) Schematic model of the system during QM calculations: atoms that are bordering with the *DMD-only* domain are frozen and their valences are saturated with hydrogen atoms. A portion of the substrate is shown bound to the metal center.

starts with the DMD phase, which operates on most of the protein, including the backbone, except for the *QM-only* region. The temperature was ramped to 0.20 kcal/(mol*K) and then decreased stepwise (5 steps, consisting of 500 t.u. each) to anneal and equilibrate the structure. Annealing was found to help achieve better sampling and statistics of the resulting ensemble. After equilibration, the temperature is kept low for 10,000 t.u., and at this stage, data are collected. The DMD-produced ensemble is clustered according to geometric similarity, based on the Kabcsh[27] RMSD for all pairwise snapshot structures and by applying a hierarchical clustering algorithm.[28] For each cluster, both the structure closest to the centroid and the one with the lowest DMD energy were used as representatives for the QM phase.

Following each iteration, the *QM-DMD* domain is extracted from each of the centroid and low-energy structures, capped with hydrogens, and a single-point QM energy is calculated for it. For the QM calculations, DFT is used in the specific BP86[29–33] and formulation of the exchange and correlation functional. A double ζ quality basis set (def2-SVP)[34] for H, C, N, O, and S and a triple ζ quality basis set (def2-TZVPP)[35] for the metals were used. Resolution of identity[36] and multipole accelerated resolution of identity[37] as implemented in *Turbomole*[38] were exploited to speed up the calculations. Empirical dispersion correction for DFT calculations was included in both energy and gradient evaluations.[39] Solvent was included via the Conductor-like Screening Model (COSMO) continuum solvent with the dielectric constant set to 20.0.[40] After that, the structures are scored, based on both the QM energy of the *QM-DMD* region and the DMD energy.[12] A single structure is selected from each iteration, and it is partially optimized at the QM level with constraints fixing the points of attachment to the rest of the protein. Then, the active site is reinstalled into the protein, the QM/DMD boundary shrinks again to go around just the *QM-region*, and the simulation proceeds with the new DMD phase, when the structural information of the active site can be propagated to the rest of the protein. The overall QM/DMD simulation for each protein runs until convergence, and in this work, 20 iterations were enough, corresponding to approximately 10.5 ns of dynamics. From each run, the structure with the lowest QM energy was selected for the mechanistic study.

Methods used in the mechanistic study

Staying consistent with the level of theory with the QM optimizations during the QM/DMD simulations, all stationary points along the reaction profile were calculated with the BP86 functional plus empirical dispersion and a double ζ quality basis set (def2-SVP) for H, C, N, O, and S and a triple ζ quality basis set (def2-TZVPP) for the iron and nickel. All calculations included the solvation via COSMO with the dielectric constant set to 20.0. The nature of each stationary point was confirmed with a frequency calculation: no imaginary frequencies confirmed the local minima, and one imaginary frequency with the normal mode going along the reaction coordinate confirmed TSs. Additionally, TPSSh[41]/def2-TZVPP and B3LYP[42,43]/def2-TZVPP with empirical dispersion and implicit solvation were used to calculate the energies of the stationary points. The results reported in the main text are obtained with TPSSh, and those obtained with the BP86 and B3LYP functionals are given in the Supporting Information (Table S1 and S2). All charges were computed using NPA at the TPSSh/def2-TZVPP level of theory.

Supporting Information is available on reaction energy profiles calculated using a variety of DFT functionals, computed UV–Vis spectra for the substrate in solution and bound to the Fe and Ni ARD in the five- and six-membered modes, and the overlay of the QM/DMD equilibrated Ni and Fe ARD with Trp161 at the C-terminus.

Acknowledgements

This work was supported by the DARPA Young Faculty Award N66001-11-1-4138 (A.N.A.) and the National Science Foundation Graduate Fellowship #2011115747 (C.E.V.). We also thank Professor Charles Knobler (University of California, Los Angeles) for helpful discussions and his invaluable support.

Supplementary Data

Supplementary data to this article can be found online at http://dx.doi.org/10.1016/j.jmb.2013.05.001

Received 14 February 2013;
Received in revised form 27 April 2013;
Accepted 5 May 2013
Available online 13 May 2013

Keywords:
methionine salvage pathway;
metalloenzyme;
QM/DMD;
density functional theory

†M.S. and C.E.V. contributed equally to this work.

Abbreviations used:
ARD, acireductone dioxygenase; DFT, density functional theory; NPA, natural population analysis; PDB, Protein Data Bank.

References

1. Myers, W. R., Wray, J. W., Fish, S. & Abeles, R. H. (1993). Purification and characterization of an enzyme involved in oxidative carbon–carbon bond cleavage reactions in the methionine salvage pathway of *Klebsiella pneumoniae*. *J. Biol. Chem.* **268**, 24785–24791.
2. Oram, S. W., Ai, J., Pagani, G. M., Hitchens, M. R., Stern, J. A., Eggener, S. *et al.* (2007). Expression and function of the human androgen-responsive gene *ADI1* in prostate cancer. *Neoplasia*, **9**, 643–651.
3. Dai, Y., Wensink, P. C. & Abeles, R. H. (1999). One protein, two enzymes. *J. Biol. Chem.* **274**, 1193–1195.
4. Pochapsky, T. C., Ju, T., Dang, M., Beaulieu, R., Pagani, G. M. & OuYang, B. (2007). In *Metal Ions in Life Sciences* (Sigel, A., Sigel, H. & Sigel, R. K. O., eds), 2, pp. 473–500 Wiley-VCH, Weinheim, Germany.
5. Al-Mjeni, F., Ju, T., Pochapsky, T. C. & Maroney, M. J. (2002). XAS investigation of the structure and function of Ni in acireductone dioxygenase. *Biochemistry*, **41**, 6761–6769.
6. Dai, Y., Pochapsky, C. T. & Abeles, H. R. (2001). Mechanistic studies of two dioxygenases in the methionine salvage pathway of *Klebsiella pneumoniae*. *Biochemistry*, **40**, 6379–6387.
7. Chai, S., Ju, T., Dang, M., Goldsmith, R., Maroney, M. J. & Pochapsky, T. C. (2008). Characterization of metal binding in the active sites of acireductone dioxygenase isoforms from *Klebsiella* ATCC 8724. *Biochemistry*, **47**, 2428–2438.
8. Ye, S., Riplinger, C., Hansen, A., Krebs, C., Bollinger, J. M., Jr. & Neese, F. (2012). Electronic structure analysis of the oxygen-activation mechanism by Fe^{II}- and α-ketoglutarate (αKG)-dependent dioxygenases. *Chem. Eur. J.* **18**, 6555–6567.
9. Christian, J. G., Ye, S. & Neese, F. (2012). Oxygen activation in extradiol catecholate dioxygenases—a density functional study. *Chem. Sci.* **3**, 1600–1611.
10. Wray, W. J. & Abeles, H. R. (1993). Purification and characterization of an enzyme involved in oxidative carbon–carbon bond cleavage reactions in the methionine salvage pathway of *Klebsiella pneumoniae*. *J. Biol. Chem.* **268**, 21466–21469.
11. Wray, W. J. & Abeles, H. R. (1995). The methionine salvage pathway in *Klebsiella pneumoniae* and rat liver. Identification and characterization of two novel dioxygenases. *J. Biol. Chem.* **270**, 3147–3150.
12. Borowski, T., Bassan, A. & Siegbahn, P. E. M. (2006). DFT study of the uncatalyzed dioxygenation of acireductone. *J. Mol. Struct. Theochem.* **772**, 89–92.
13. Sparta, M., Ding, F., Shirvanyants, D., Dokholyan, N. V. & Alexandrova, A. N. (2012). Hybrid dynamics simulation engine for metalloproteins. *Biophys. J.* **103**, 767–776.
14. Allpress, C. J., Grubel, K., Szajna-fuller, E., Arif, M. A. & Berreau, L. (2013). Regioselective aliphatic carbon–carbon bond cleavage by a model system of relevance to iron-containing acireductone dioxygenase. *J. Chem. Soc.* **135**, 659–668.
15. Ju, T., Goldsmith, R., Chai, S., Maroney, M. J., Pochapsky, S. S. & Pochapsky, T. C. (2006). One protein, two enzymes revisited: a structural entropy switch interconverts the two isoforms of acireductone dioxygenase. *J. Mol. Biol.* **393**, 823–834.
16. Reed, A. E., Weinstock, R. B. & Weinhold, F. (1985). Natural population analysis. *J. Chem. Phys.* **83**, 735–746.
17. Pochapsky, T. C., Pochapsky, S. S., Ju, T., Hoefler, C. & Liang, J. (2006). A refined model for the structure of acireductone dioxygenase from *Klebsiella ATCC 8724* incorporating residual dipolar couplings. *J. Biomol. NMR*, **34**, 117–127.
18. Dokholyan, N. V., Buldyrev, S. V., Stanley, H. E. & Shakhnovich, E. I. (1998). Molecular dynamics studies of folding of a protein-like model. *Fold. Des.* **3**, 577–587.
19. Dokholyan, N. V. (2006). Studies of folding and misfolding using simplified models. *Curr. Opin. Struct. Biol.* **16**, 79–85.
20. Ding, F., Guo, W. H., Dokholyan, N. V., Shakhnovich, E. I. & Shea, J. E. (2005). Reconstruction of the src-SH3 protein domain transition state ensemble using multiscale molecular dynamics simulations. *J. Mol. Biol.* **350**, 1035–1050.
21. Ding, F., Tsao, D., Nie, H. & Dokholyan, N. V. (2008). Ab initio folding of proteins with all-atom discrete molecular dynamics. *Structure*, **16**, 1010–1018.
22. Sparta, M. & Alexandrova, A. N. (2012). How metal substitution affects the enzymatic activity of catechol-*O*-methyltransferase. *PLoS One*, **7**, e47172.
23. Valdez, C. E. & Alexandrova, A. N. (2012). Why urease is a di-nickel enzyme whereas the CcrA β-lactamase is a Di-Zinc enzyme. *J. Phys. Chem. B*, **116**, 10649–10656.
24. Valdez, C. E., Sparta, M. & Alexandrova, A. N. (2012). The role of the flexible L43–S54 protein loop in the CcrA metallo-β-lactamase in binding structurally dissimilar β-lactam antibiotics. *J. Chem. Theor. Comput.* **9**, 730–737.
25. Andersen, H. C. (1980). Molecular dynamics simulations at constant pressure and/or temperature. *J. Chem. Phys.* **72**, 2384–2393.
26. Ramachandran, S., Kota, P., Ding, F. & Dokholyan, N. V. (2011). Automated minimization of steric clashes in protein structures. *Proteins*, **79**, 261–270.
27. Kabsch, W. (1976). A solution for the best rotation to relate two sets of vectors. *Acta Crystallogr., Sect. A*, **32**, 922–923.
28. Barton, G. J. OC—A cluster analysis program, University of Dundee, Scotland, UK (1993, 2002), www.compbio.dundee.ac.uk/downloads/oc.
29. Dirac, P. A. M. (1929). Quantum mechanics of many-electron systems. *Proc. Royal Soc. (London) A*, **123**, 714.
30. Slater, J. C. (1951). A simplification of the Hartree–Fock method. *Phys. Rev.* **81**, 385–390.
31. Vosko, S. H., Wilk, L. & Nusair, M. (1980). Accurate spin-dependent electron liquid correlation energies for local spin density calculations: a critical analysis. *Can. J. Phys.* **80**, 1200–1211.
32. Becke, A. D. (1988). Density-functional exchange-energy approximation with correct asymptotic behavior. *Phys. Rev. A*, **38**, 3098–3100.
33. Perdew, J. P. (1986). Density-functional approximation for the correlation energy of the inhomogeneous electron gas. *Phys. Rev. B*, **33**, 8822–8824.
34. Schafer, A., Horn, H. & Ahlrichs, R. (1992). Fully optimized contracted gaussian basis sets for atoms Li to Kr. *J. Chem. Phys.* **97**, 2571–2577.

35. Weigend, F. & Ahlrichs, R. (2005). Balanced basis sets of split valence, triple zeta valence and quadruple zeta valence quality for H to Rn: design and assessment of accuracy. *Phys. Chem. Chem. Phys.* **7**, 3297–3305.
36. Arnim, M. V. & Ahlrichs, R. (1998). Performance of parallel TURBOMOLE for density functional calculations. *J. Comput. Chem.* **19**, 1746–1757.
37. Sierka, M., Hogekamp, A. & Ahlrichs, R. (2003). Fast evaluation of the coulomb potential for electron densities using multipole accelerated resolution of identity approximation. *J. Chem. Phys.* **118**, 9136–9148.
38. Turbomole V6.3 2011, a development of University of Karlsruhe and Forschungszentrum Karlsruhe GmbH, 1989–2007, Turbomole GmbH, since 2007, available from http://www.turbomole.com.
39. Grimme, S. (2004). Accurate description of van der Waals complexes by density functional theory including empirical corrections. *J. Comput. Chem.* **25**, 1463–1473.
40. Klamt, A. & Schüürmann, G. J. (1993). COSMO: a new approach to dielectric screening in solvents with explicit expressions for the screening energy and its gradient. *J. Chem. Soc. Perkin Trans. 2*, **5**, 799–805.
41. Staroverov, V., Scuseria, G., Tao, J. & Perdew, J. (2003). Comparative assessment of a new nonempirical density functional: molecules and hydrogen-bonded complexes. *J. Chem. Phys.* **119**, 12129–12137.
42. Becke, A. D. (1993). Density-functional thermochemistry. III. The role of exact exchange. *J. Chem. Phys.* **98**, 5648–5652.
43. Grimme, S., Antony, J., Ehrlich, S. & Krieg, H. (2010). A consistent and accurate *ab initio* parametrization of density functional dispersion correction (DFT-D) for the 94 elements H-Pu. *J. Chem. Phys.* **132**, 154104.